# A Novel Global Grid Model for Atmospheric Weighted Mean Temperature in Real-Time GNSS Precipitable Water Vapor Sounding

Liangke Huang, Zhedong Liu, Hua Peng, Si Xiong, Ge Zhu, Fade Chen, Lilong Liu, and Hongchang He

***Abstract*—The atmospheric weighted mean temperature (Tm) is an important parameter in calculating the precipitable water vapor from Global Navigation Satellite System (GNSS) signals. As both GNSS positioning and GNSS precipitable water vapor detection require high spatial and temporal resolutions for calculating Tm, high-precision modeling of Tm has gained widespread attention in recent years. The previous models for calculating Tm have the limitation of too many model parameters or single-grid data. Therefore, this study presents a global high-precision Tm model (GGTm-H model) developed from the latest Modern-Era Retrospective Analysis for Research and Applications, version-2 (MERRA-2) atmospheric reanalysis data provided by the United States National Aeronautics and Space Administration. The accuracy of the GGTm-H model was verified by combining the MERRA-2 surface Tm data and 319 radiosonde data. The results highlighted that 1) When the MERRA-2 Tm data were used as a reference value, the mean annual RMSE of the GGTm-H model was observed to be 2.72 K. When compared with the Bevis model, GPT2w-5 model, and GPT2w-1 model, the GGTm-H model showed an improvement of 1.5, 0.33, and 0.21 K, respectively. 2) When the radiosonde data were used as a reference value, the mean bias and RMSE of the GGTm-H model were −0.41 K and 3.82 K, respectively. Compared with the other models, the GGTm-H model had the lowest mean annual bias and RMSE. The developed model does not consider any meteorological parameters while calculating Tm. Therefore, it has important applications in the real-time and high-precision monitoring of precipitable water vapor from GNSS signals.**

***Index Terms*—Atmospheric weighted mean temperature (Tm), Global Navigation Satellite System (GNSS), precipitable water vapor (PWV), Tm lapse rate.**

Manuscript received 27 September 2022; revised 28 January 2023 and 20 February 2023; accepted 16 March 2023. Date of publication 24 March 2023; date of current version 7 April 2023. This work was funded in part by the National Natural Science Foundation of China under Grants 41704027 and 41864002, in part by the Guangxi Natural Science Foundation of China under Grant 2020GXNSFBA297145, in part by the "Ba Gui Scholars" Program of the provincial government of Guangxi, and in part by the Innovation Project of GuangXi Graduate Education under Grant YCSW2022322. *(Corresponding authors: Ge Zhu; Fade Chen.)*

Liangke Huang, Zhedong Liu, Hua Peng, Ge Zhu, Fade Chen, Lilong Liu, and Hongchang He are with the College of Geomatics and Geoinformation, Guilin University of Technology, Guilin 541004, China (e-mail: lkhuang666@163.com; lzd@glut.edu.cn; penghua@glut.edu.cn; zhuge@glut.edu.cn; fadechen-666@163.com; hn_liulilong@163.com; hhe@glut.edu.cn).

Si Xiong is with the Hubei University of Science and Technology, Xianning 437100, China (e-mail: xs-man@foxmail.com).

Digital Object Identifier 10.1109/JSTARS.2023.3261381

## I. Introduction

WATER vapor makes up a small part of the atmosphere, but it plays a key role in a range of weather phenomena, from heavy rains to droughts [1], [2]. Precipitable water vapor (PWV) refers to the precipitation generated by the total amount of PWV contained in the large air column of a unit section from the ground to the top of the atmosphere, all of which condenses to the ground, which is an important parameter reflecting the change of atmospheric PWV [3], [4]. With the development of Global Navigation Satellite System (GNSS) technology, ground-based GNSS inversion can obtain PWV with higher temporal and spatial resolution, which has become one of the important means for PWV monitoring [5], [6], [7], [8], [9], [10], [11], [12]. Recently, high-precision GNSS PWV have played an important role in the monitoring and analysis of extreme weather such as heavy rain and typhoons [13], [14], [15].

The atmospheric weighted mean temperature (Tm) is a key parameter for calculating GNSS vapor conversion coefficient [16], [17], [18], [19], [20]. High-precision and real-time Tm values can be obtained by integrating the atmospheric reanalysis data; however, the data update is slow with limited horizontal resolution. This significantly restricts the development and application of GNSS meteorology in global regions [21], [22], [23], [24]. In recent years, several researchers have developed many regional or global Tm models to satisfy the needs of PWV inversion. The well-known Bevis model was originally developed for a specific area (27°N–65°N) in the northern hemisphere [25]. These models show good accuracy in a specific area but are not suitable for GNSS-based PWV estimation over a large area. Zhang et al. [26] observed that lapse rate is an important parameter for Tm elevation correction and developed an enhanced Tm model for China (GH-Tm). Studies by Huang et al. [27], [28] indicated that large topographic fluctuations in China lead to significant systematic error in the GPT2w-1 model [29] valuation. Therefore, the IGPT2W model was developed based on the lapse rate. Compared with the GPT2w model, the improved model has enhanced accuracy in high-altitude areas. Yao et al. [30], [31], [32] used spherical harmonics to develop a globally applicable empirical Tm model, GWMT GTm-III. This model considers the height and the periodicity of Tm. Yao et al. [33] considered the approximately linear relationship between the atmospheric weighted temperature and temperature and used

the globally applicable ECMWF to establish the Tm model. The large-scale data involved in modeling and the very large selected grid range affect the stability of the model to some extent at a global level. Based on the Bevis model, Jiang et al. [34] considered the temporal variations in Ts–Tm for each Ts–Tm grid data and developed a global grid Ts–Tm model. Similarly, Sun et al. [35] developed a global Tm model considering nonmeteorological parameters (GTrop model). Although this model has good accuracy, too many model parameters make the model complicated and limit its practical applications to some extent. Yao et al. [36] used the ECMWF products to analyze the Tm distribution characteristics in the vertical direction and developed a new global Tm model. Tested with the ECMWF and the radiosonde (RS) data, the RMS of the model is 3.84 and 4.36 K, respectively, achieving accuracy improvements of 27% and 20% compared to the existing model. Sun et al. [37] developed a new global grid-based Tm empirical model named GGNTm. A three-order polynomial function was utilized to fit the vertical nonlinear variation in Tm at the grid points. The model made significant improvements at high-altitude pressure levels. Cao et al. [38] proposed to correct the bias of the GRAPES_MESO forecasting data using a linear model and a spherical cap harmonic model. Compared to the existing empirical models that only capture the tidal variations, the CTropGrid products capture well the nontidal variations of Tm.

Although the above-mentioned Tm empirical models show their advantages, some limitations still exist, such as the adoption of only single gridded data for modeling, and the model parameters need to be further optimized. Therefore, it is of great importance to develop a novel global Tm grid model for real-time GNSS PWV sounding. A sliding window algorithm is introduced to divide the global into regular windows of the same size, and the Modern-Era Retrospective Analysis for Research and Applications, version-2 (MERRA-2) data are adopted in the calculation of Tm information.

## II. Data and Methods

### A. Data

MERRA-2 is the latest atmospheric reanalysis produced by the United States National Aeronautics and Space Administration (NASA). MERRA-2 provides pressure-level data and single-level data. The horizontal resolution of the stratified data is 0.5° × 0.625° (latitude × longitude), the time resolution is 6 h (UTC 00:00, 06:00, 12:00, and 18:00), and the vertical resolution is 42 layers (top-level height is about 50 km). The horizontal resolution of the surface data is also 0.5° × 0.625°, and the time resolution is 1 h (UTC 00:00, 01:00, …,23:00).

RS data are important meteorological observation data, with observations typically made only twice a day (UTC 0:00 and UTC 12:00). At present, there are more than 1500 comprehensive sounding stations. Each sounding station provides layered data on atmospheric pressure, temperature, relative humidity, and other meteorological parameters and surface parameters such as atmospheric PWV from the surface to the near-earth space extending about 30 km above [39]. Since the sounding data are obtained through actual measurements, they have reliable accuracy and, hence, are widely used in the model construction and accuracy verification analysis of key troposphere parameters, such as Tm.

### B. Methods

Since the MERRA-2 reanalysis data with the horizontal resolution of 0.5° × 0.625° (latitude × longitude) are used for modeling, the global region was first divided to obtain a grid consistent with the horizontal resolution of the MERRA-2 reanalysis data. The sliding window algorithm [40], [41], [42] is applied to obtain the tropospheric model parameters in the window.

The integral method is used to calculate the Tm value within the stratified height-range MERRA-2 reanalysis data. The basic formula can be expressed as follows:

$$T_m = \frac{\int_{h_L}^{h_{\text{top}}} \left(\frac{e}{T}\right) dH}{\int_{h_L}^{h_{\text{top}}} \left(\frac{e}{T^2}\right) dH} = \frac{\sum \left(\frac{e_i}{T_i}\right) \Delta H_i}{\sum \left(\frac{e_i}{T_i^2}\right) \Delta H_i} \tag{1}$$

where $e$ denotes the water vapor pressure (hPa), $T$ is the temperature (K), and $e_i$ is the average water vapor pressure of layer i of the atmosphere. $T_i$ is the average temperature of layer i of the atmosphere. $\Delta H_i$ is the thickness of the i layer of the atmosphere. $h_{\text{top}}$ and $h_L$ are the top and bottom heights of the hierarchical data integration calculation, respectively.

As shown in Fig. 1, Tm data from 545 RS stations in 2017 were used to evaluate the accuracy of Tm calculated from the MERRA-2 reanalysis data based on the annual mean bias and RMSE.

As depicted in Fig. 1, the overall bias of Tm calculated from the MERRA-2 reanalysis data was close to 0, and the absolute bias values of most measurement stations were within 1 K. The high-latitude stations had the maximum positive bias and are centrally distributed in Asia. A small negative bias was observed in the equatorial and low-latitude regions, whereas Antarctic stations had the largest negative bias. Overall, the Tm calculated from the MERRA-2 reanalysis data showed a narrow global distribution, indicating that the Tm obtained through MERRA-2 data integration has reliable accuracy. The Tm calculated from the MERRA-2 reanalysis data showed the largest RMSE value in Greenland and Asia. This may be due to the relatively skewed spatial and temporal distribution of Tm in the high latitudes. The Tm obtained from MERRA-2 data integration showed a small RMSE in other regions, implying that the Tm calculated from the MERRA-2 reanalysis data has high accuracy and can be used for the construction of the Tm lapse rate model and the weighted average temperature model.

Due to the difference between the user's location and the elevation of the grids, large errors will be caused when used directly. Therefore, it is important to assess the spatiotemporal characteristics of the Tm lapse rate on a global scale. The Tm stratified data of the global region from 2014 to 2017 were calculated from the MERRA-2 reanalysis data at 0.5° × 0.625° and then analyzed by the changes in Tm values with height. The reanalysis data at three resolutions (89.5°N × 179.375°W, 89°N × 178.75°W, and 88°N × 177.5°W) dated January 1 and

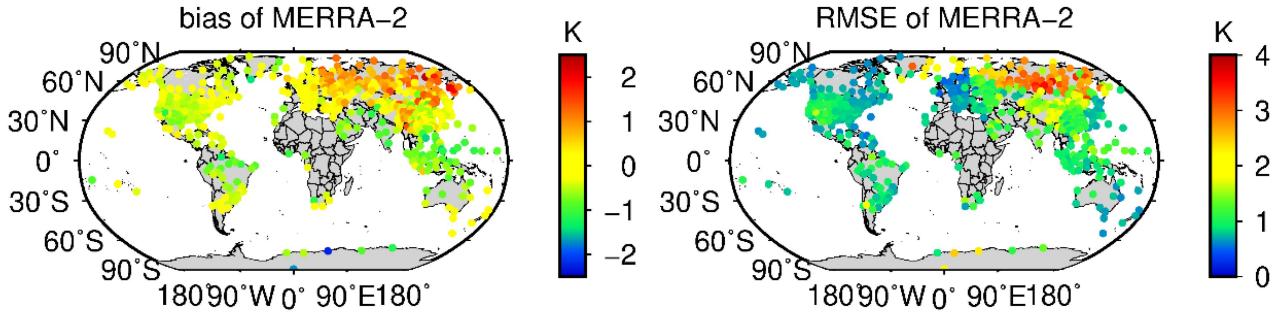


Fig. 1. Accuracy of Tm calculated from the 2017 MERRA-2 data.

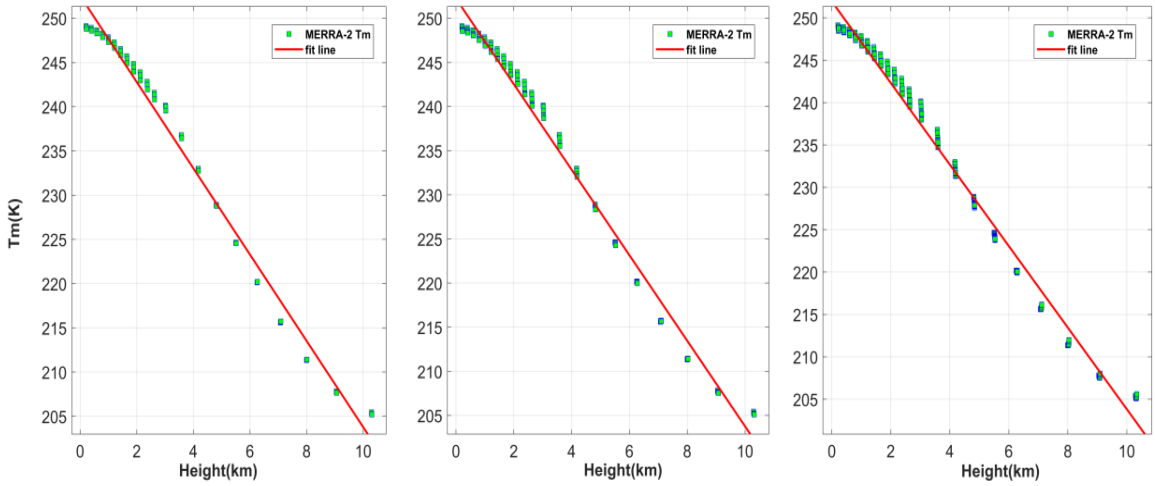


Fig. 2. Fitting graph of Tm lapse rate coefficients of grid window center at the three resolutions. (a) 89.5°N 179.375°W. (b) 89°N 178.75°W. (c) 88°N 177.5°W.

the window center grid data were selected, and the changes in Tm with height were observed. As shown in Fig. 2, the distribution in MERRA-2 layered Tm and elevation were almost linear. Tm showed a declining trend with increased elevation, and its slope is the lapse rate of Tm, which can be expressed as follows:

$$T_m = \gamma \times h + k \tag{2}$$

where $\gamma$ denotes the lapse rate of Tm, $h$ is the height, and $k$ is the constant. To obtain the lapse rate of Tm, the Tm profile information at 9/25/81 lattice outlets and the corresponding bit potential height data were fitted to each window at the three global horizontal resolutions.

Four representative lattice outlets were selected to assess the temporal variations in the lapse rate coefficient. The Tm lapse rates from 2014 to 2017 were analyzed to obtain the periodic characteristics of the Tm lapse rate.

As observed in Fig. 3, the lapse rate of Tm showed a significant periodic change, which was consistent with the vertically decreasing rate of Tm, as observed in previous studies [43], [44].

The Tm stratified data were calculated by the integration of the hierarchical meteorological parameters at 0.5° × 0.625° obtained from the MERRA-2 reanalysis data. Furthermore, the Tm lapse rate was subsequently obtained by analyzing the changes in the Tm values with height. As shown in Fig. 4, the color bar shows that the lapse rate of Tm had the largest absolute value near the equator, indicating drastic changes in Tm near the equator with height. The absolute value of Tm at high latitudes was small, indicating a relatively small change in Tm with height.

## III. Results and Discussion

### A. Construction of the Global Tm Lapse Rate Model

The lapse rate of Tm can effectively improve the vertical accuracy of Tm at different heights. Therefore, evaluating the lapse rate of $T_m$ can provide valuable reference for developing a high-precision $T_m$ model. As the sliding window algorithm effectively improves the application efficiency of the reanalysis data, the limitations of using a single-lattice-dot data modeling are avoided. The optimization of the $T_m$ lapse rate model application in spatial interpolation and the improvement in the height-corrected efficiency of the $T_m$ lapse rate model were obtained by linearly fitting the $T_m$ stratified data and bit-high potential data of MRERRA-2 from nine grid outlets in each window to obtain the $T_m$ lapse rate in that window. Furthermore, the analysis of spatial and temporal changes in the Tm lapse rate highlighted that the lapse rate of $T_m$ was mainly manifested in the annual and semiannual cycle characteristics. The model can

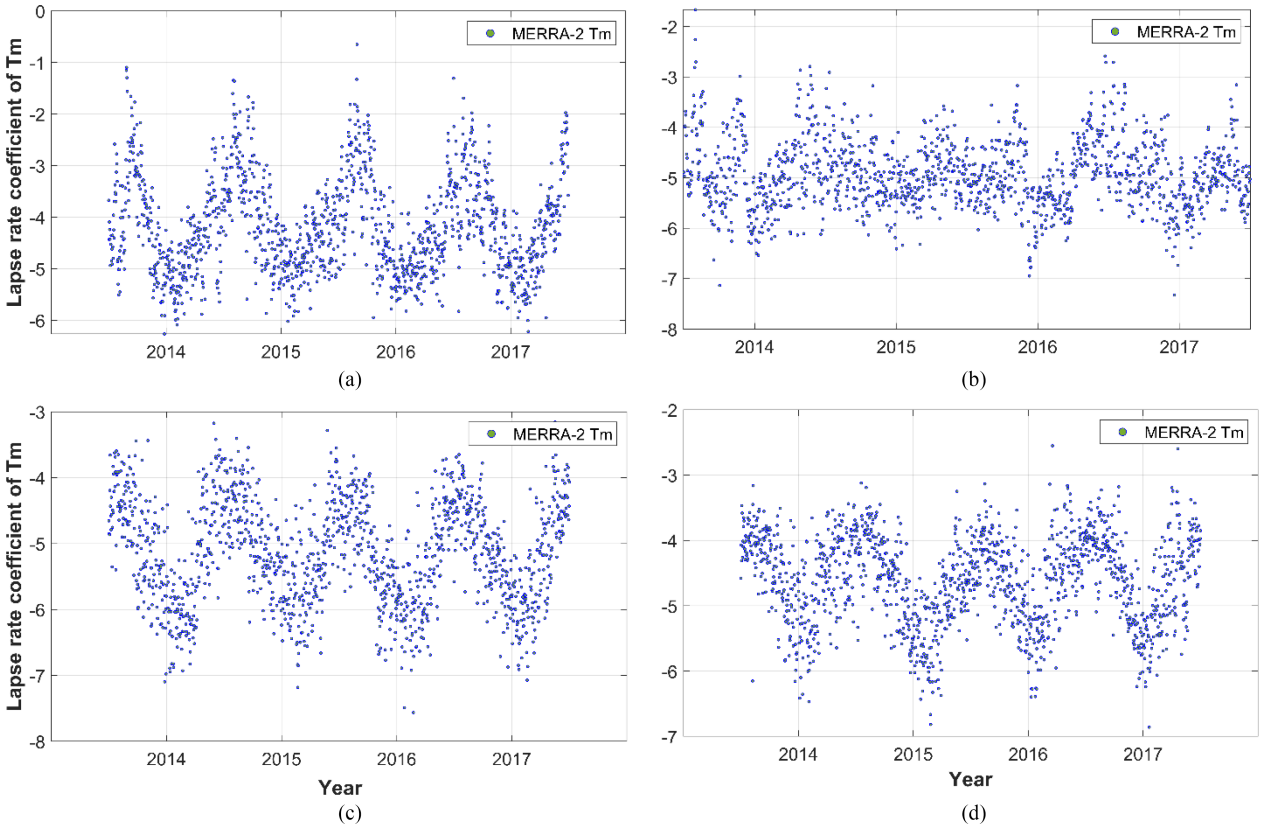


Fig. 3. Changes in Tm with respect to the lapse rate coefficient of Tm and year. (a) 60°N 90°W. (b) 60°N 90°E. (a) 60°S 90°W. (a) 60°S 90°E.

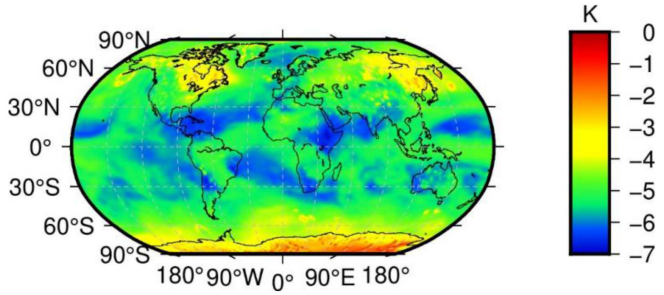


Fig. 4. Spatial distributions of the global Tm lapse rate.

be expressed as follows:

$$T_{ma} = \gamma \times (h_a - h_b) + T_{mb} \tag{3}$$

where $\gamma$ denotes the lapse rate of Tm; $h_a$ and $h_b$ denote the target height and reference height, respectively; $T_{ma}$ and $T_{mb}$ denote the Tm value of the target height and reference height, respectively.

The lapse rate of $T_m$ under each window can be expressed separately using the following equation:

$$\gamma = a_0 + a_1 \cos\left(2\pi \frac{\text{doy}}{365.25}\right) + a_2 \sin\left(2\pi \frac{\text{doy}}{365.25}\right) + a_3 \cos\left(4\pi \frac{\text{doy}}{365.25}\right) + a_4 \sin\left(4\pi \frac{\text{doy}}{365.25}\right) \tag{4}$$

where doy represents the day of the year, $a_0$ represents the annual mean of the Tm lapse rate, and $(a_1, a_2)$ and $(a_3, a_4)$ indicate the annual and semiannual cycle coefficients of the Tm lapse rate, respectively. In each window globally, the coefficients are estimated based on the Tm layered profile information at the nine MERRA-2 grid points contained in the window at a resolution of 6 h through least-squares adjustment. The five vertical reduction rates of Tm at the center point of each window can be calculated globally, and the coefficient factors can be stored in the form of lattice points in the geometric center of each window. The effect of the Tm lapse rate model on Tm vertical correction was evaluated using Tm stratified data at three resolutions. The corresponding bit-high potential data were then selected to fit the Tm lapse rate model. According to the sliding window algorithm, the global region was divided into three horizontal resolutions of 1° × 1.25°, 2° × 2.5°, and 4° × 5°, and the Tm data and the corresponding bit-high potential data in the global region from 2014 to 2017 were used to develop the Tm lapse rate models, namely, the Tm-H, Tm-H2, and Tm-H4 models, respectively. Considering that Tm vertical correction is mainly applied to the lower layers of the atmosphere, the height range from the surface to 10 km was chosen for the stratified data while fitting the Tm lapse rate.

Fig. 5 represents the annual average of the Tm lapse rate coefficient, the annual periodic amplitude, and the semiannual amplitude distributions at the three horizontal resolutions. As shown in Fig. 5, the differences between the annual average,

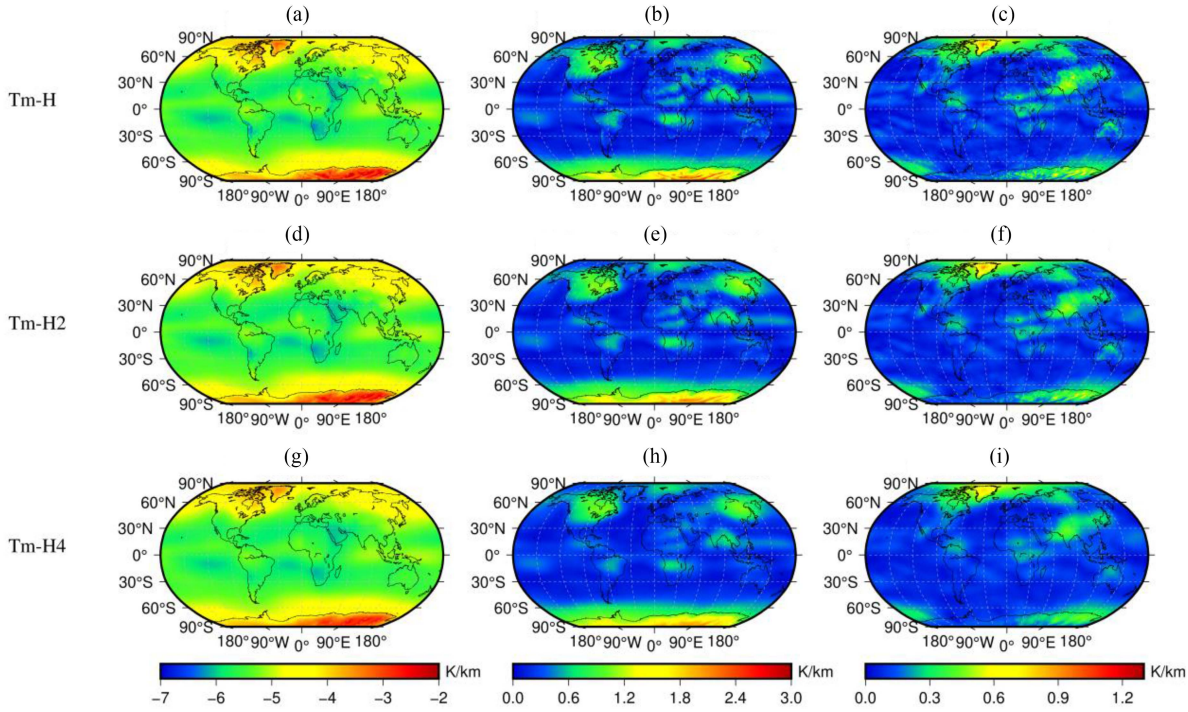


Fig. 5. Distribution of the (a), (d), (g) annual average of the lapse rate coefficients and (b, (e), (h) annual periodic amplitude and (c), (f), (i) semiannual amplitude at the center of the global grid window for the three resolutions.

annual periodic amplitude, and semiannual periodic amplitude distributions of the Tm-H and Tm-H2 model coefficients were not evident. The Tm lapse rate was calculated from the reanalysis data at $2° \times 2.5°$ horizontal resolution to reduce the usage parameters of the model. Moreover, the Tm-H4 model was evaluated at a horizontal resolution of $4° \times 5°$ due to the large window size. The annual periodic signal and semiannual signal intensities were weakened while using the Tm profile information from 81 lattice outlets in the window, resulting in relatively small changes in the annual periodic amplitude and semiannual amplitude. The absolute annual averages of Tm-H and Tm-H2 models were large in low and middle latitudes compared to those in high latitudes and bipolar regions. The lowest annual mean was observed in Greenland and Antarctica, indicating relatively drastic changes in Tm in the low and middle latitudes and relatively moderate changes in the high latitudes. Large annual and semiannual periodic amplitudes were observed in some parts of Europe, Eastern China, Central Africa, Antarctica, and North America due to the stronger seasonal variation in Tm at the higher latitudes. Therefore, the model coefficient amplitude showed large values. The annual periodic amplitude and semiannual periodic amplitude were relatively large, probably due to the polar phenomenon. However, the variations in the average annual periodic amplitude and semiannual periodic amplitude of the Tm-H4 model were relatively small, which may affect the application of the Tm lapse rate for elevation correction.

*1) Accuracy Test of the Tm Lapse Rate Model:* To evaluate the application of the Tm lapse rate models for elevation correction at three horizontal resolutions, the surface Tm grid products of the 2017 MERRA-2 reanalysis data were initially selected.

TABLE I
COMPARISON OF ACCURACY OF THE THREE RESOLUTION GRIDS VERIFIED USING HIERARCHICAL MERRA-2 GRID TM DATA (UNIT, K)

| Models | | Tm-H | Tm-H2 | Tm-H4 |
|---|---|---|---|---|
| bias | Max | 3.12 | 2.71 | 2.23 |
| | Min | −5.75 | −5.51 | −5.33 |
| | Mean | −0.70 | −0.70 | −0.70 |
| RMSE | Max | 5.47 | 5.38 | 5.34 |
| | Min | 0.63 | 0.15 | 0.09 |
| | Mean | 3.27 | 3.26 | 3.26 |

Furthermore, the Tm lapse rate model output corresponding to the hierarchical Tm grid at three horizontal resolutions was corrected, and the MERRA-2 stratified Tm products were used to verify the Tm accuracy after elevation correction, as highlighted by the values of bias and RMSE in Table I and Fig. 6.

As shown in Table I, the bias using the lapse rate function model at three resolutions is −0.7 K after applying surface MERRA-2 grid Tm products to correct the lapse rate model elevation corresponding to the hierarchical MERRA-2 grid Tm products. The RMSE of the Tm-H model was 0.01 K higher than that of the Tm-H2 and Tm-H4 models. The maximum and minimum distributions of bias and RMSE indicated that lower resolution led to better stability of the model with minimum error because of the accurate data of the Tm profile at the center point of the grid window. The lower resolution also led to increased

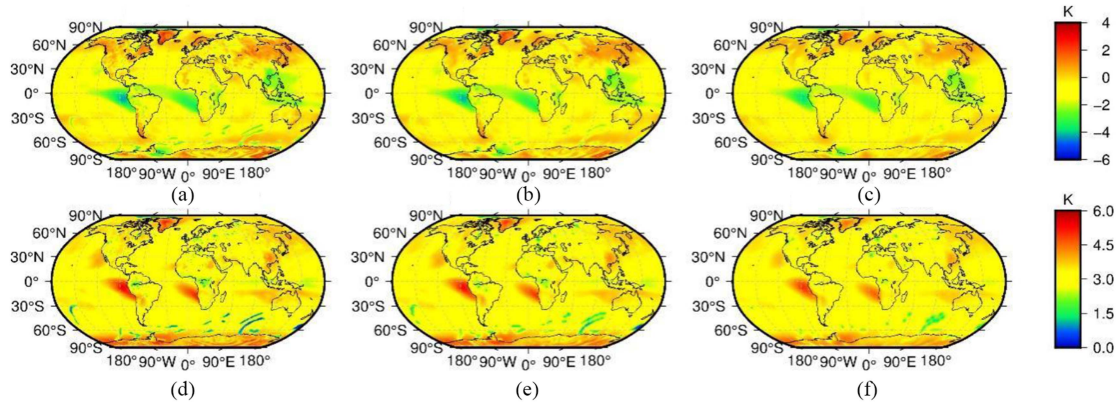


Fig. 6. Verification of bias and RMSE values for the three resolution grids using the hierarchical MERRA-2 grid Tm data. (a) Bias (Tm-H). (b) Bias (Tm-H2). (c) Bias (Tm-H4). (d) RMSE (Tm-H). (e) RMSE (Tm-H2). (f) RMSE (Tm-H4).

profile information of the window at 9/25/81. The Tm value is the value of the window center point; hence, the resolution was observed to be low, and the Tm lapse rate coefficient was found to be more stable. As shown in Fig. 6, large overall differences between the bias and the RMSE obtained by the model elevation correction results of different resolution lapse rates were not observed; however, sea–land distribution and regional distribution differences were observed. In terms of bias, it showed a significant negative bias at the equator and near the middle and low latitudes, and a large positive bias was observed in northeast China, the northern United States, Greenland, and parts of Antarctica. This indicated that the Tm values corrected by the lapse rate model were slightly larger than the MERRA-2 stratified Tm values due to the strong seasonal correction of Tm. In terms of RMSE at three resolutions, the maximum value was observed at the equator, high-latitude areas, and sea–land junction because the Tm is affected by terrain and tropical monsoon, resulting in the ideal correction effect through extrapolation of the simple linear relationship. Overall, the decreasing rate function model at all three resolutions can provide high-precision Tm values. The accuracy of bias and RMSE in specific regions was significantly enhanced with the improved resolution of the model, implying that the improvement in the horizontal resolution of the model parameters can lead to improvement in the model accuracy. Therefore, the selection of the Tm lapse rate model can provide a reference value for the spatial interpolation and the modeling of Tm.

The application of the Tm lapse rate model in elevation correction was further validated by selecting the Tm data in 2017 as the reference value to test the model's accuracy. The surface grid Tm product of MERRA-2 was corrected to the probe height for greater accuracy. As shown in Table II, the surface MERRA-2 grid Tm data were corrected to the minimum bias and RMSE of the elevation of the sounding station, namely −0.09 K and 1.47 K, respectively, using the Tm-H model. The decreasing resolution of the Tm lapse rate model led to the calculation of a larger negative bias and a gradual decrease in stability. RMSE increased by 0.21 K (14%), i.e., from 1.47 K for Tm-H to 1.68 K for Tm-H2. Similarly, RMSE increased by 0.44 K (26%), from 1.68 K for Tm-H2 to 2.12 K for Tm-H4. However, with the further expansion of the horizontal resolution, comparing the model output with the measured Tm provided by the sounding station leads to greater errors. This study temporarily considered the application of the three resolved Tm lapse rate models for elevation correction to provide users with more stable Tm values. As shown in Fig. 7, the test results of the three resolution models corrected to the sounding height were similar. Overall, most of the selected sounding sites are on land, and the distribution of these sites in the ocean is relatively sparse. Moreover, the RMSE in the marine area was low, which may be due to the distribution of sea and terrain affecting the Tm lapse rate and further affecting the vertical correction effect. The values of bias and RMSE were larger in high latitudes of the northern hemisphere, which is due to the strong seasonal variation of Tm in high latitudes. These variations are difficult to model using only the lapse rate coefficients, thus leading to large errors.

TABLE II
COMPARISON OF PRECISION FOR THE THREE RESOLUTION GRIDS VERIFIED USING THE SOUNDING TM DATA FOR 2017, (UNIT, K)

| Model | | Tm-H | Tm-H2 | Tm-H4 |
|---|---|---|---|---|
| bias | Max | 2.71 | 2.73 | 2.63 |
| | Min | −2.45 | −2.70 | −4.67 |
| | Mean | −0.09 | −0.11 | −0.12 |
| RMSE | Max | 4.64 | 4.56 | 5.24 |
| | Min | 0.70 | 0.66 | 0.76 |
| | Mean | 1.47 | 1.68 | 2.12 |

As shown in Fig. 8, considering the sounding station as the reference value and 1° × 1.25° as an example, the largest elevation of the sounding station led to a bias of about −0.5 K and an RMSE of about 2 K, indicating that the lapse rate coefficient led to a positive effect in the elevation correction. The bias and RMSE present a normal distribution form, indicating that the model lapse rate can be used for elevation correction and has good stability.

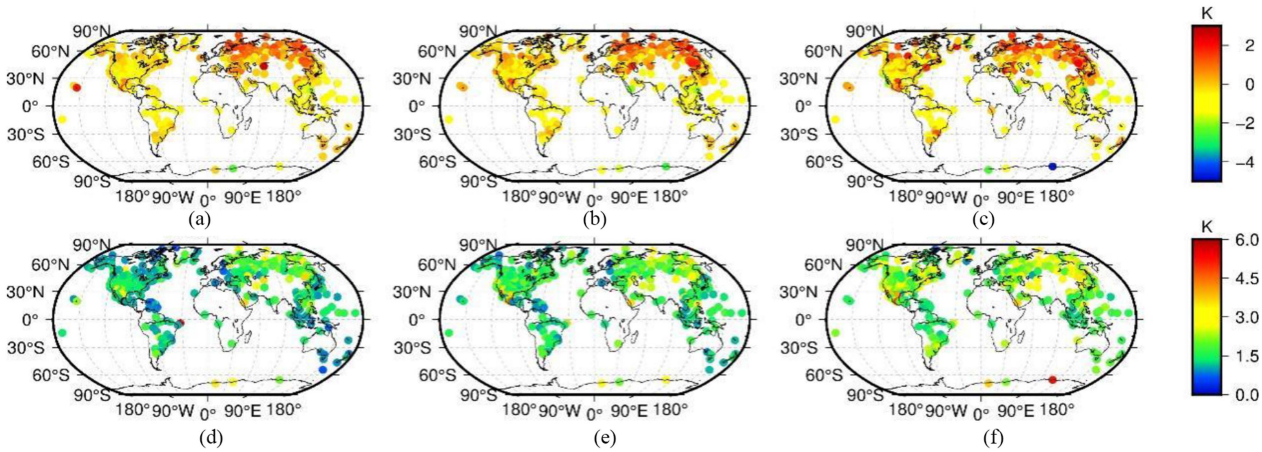


Fig. 7. Verification of bias and RMSE values for the three resolution grids using RS data. (a) Bias (Tm-H). (b) Bias (Tm-H2). (c) Bias (Tm-H4). (d) RMSE (Tm-H). (e) RMSE (Tm-H2). (f) RMSE (Tm-H4).

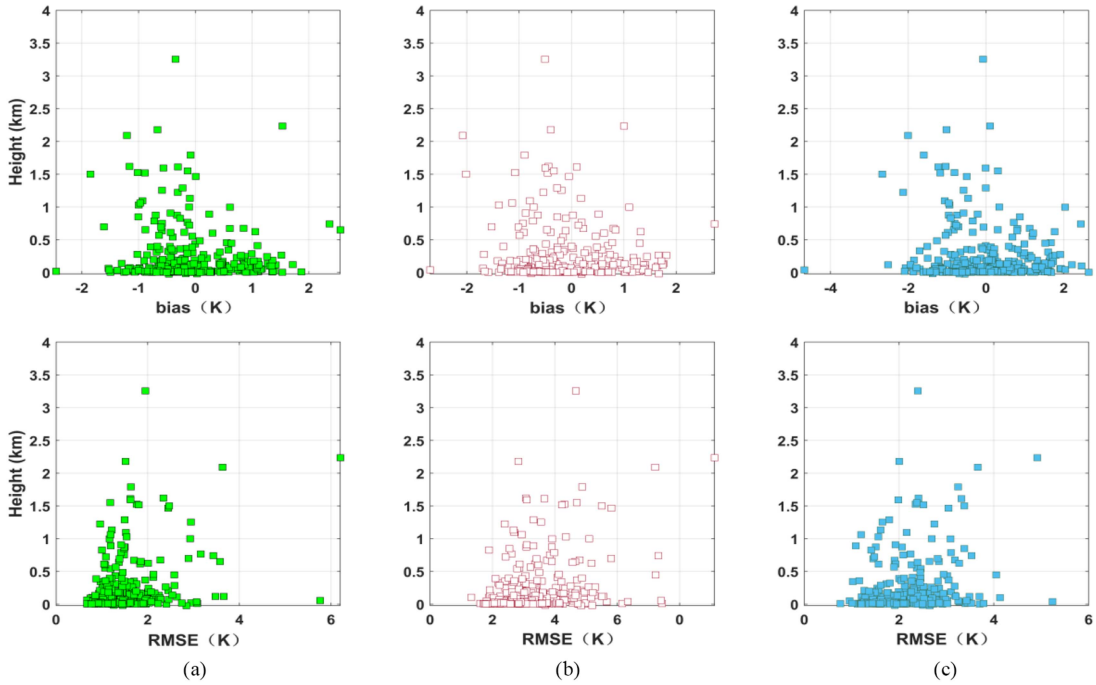


Fig. 8. Influence of sounding elevation on bias and RMSE for the three resolution grids. (a) Tm-H. (b) Tm-H2. (c) Tm-H4.

*2) Precision Analysis of the Spatial Interpolation of GGOS Atmospheric Grid Tm Products:* As GGOS can provide high-accuracy grid Tm products, this study utilized the GGOS grid Tm product correction to test the accuracy of the vertical correction model. Since the GGOS grid Tm product has only a resolution of 2° × 2.5°, the impact of two horizontal resolutions, namely, 2° × 2.5° and 4° × 5°, on the model was considered to combine the grid resolution and lapse rate model resolution.

As shown in Tables II and III and Fig. 8, the test results of the GGOS grid Tm product and surface MERRA-2 grid Tm data were found to be similar. Overall, the bias of the GGOS grid Tm product was high relative to that of the surface MERRA-2 grid products, indicating the better stability of the surface MERRA-2

TABLE III
COMPARISON OF THE PRECISION OF THE TWO RESOLUTION GRIDS VERIFIED USING PRODUCT TM DATA (UNIT, K)

| Model | | Tm-H2 | Tm-H4 |
|---|---|---|---|
| bias | Max | 2.51 | 2.84 |
| | Min | −3.06 | −4.09 |
| | Mean | 0.39 | 0.40 |
| RMSE | Max | 4.88 | 4.75 |
| | Min | 0.62 | 0.76 |
| | Mean | 1.68 | 2.12 |

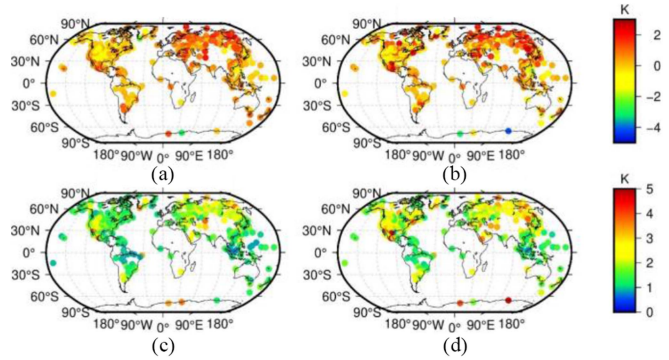


Fig. 9. Verification of the bias and RMSE of the two resolution grids using RS Tm data. (a) Bias (Tm-H2). (b) Bias (Tm-H4). (c) RMSE (Tm-H2). (f) RMSE (Tm-H4).

TABLE IV
VALIDATION ACCURACY OF THE GGTM-H, GPT2W-5, GPT2W-1, AND BEVIS MODELS BASED ON THE GLOBAL GRID VALUES OF MERRA-2 TM FOR 2015 (UNIT, K)

| Model | | Bevis | GPT2w-5 | GPT2w-1 | GGTm-H |
|---|---|---|---|---|---|
| bias | Max | 14.60 | 19.15 | 5.98 | 2.39 |
| | Min | −6.60 | −13.16 | −7.28 | −1.69 |
| | Mean | 1.55 | 0.07 | 0.06 | 0.21 |
| RMSE | Max | 15.09 | 19.48 | 7.85 | 5.35 |
| | Min | 0.91 | 0.85 | 0.67 | 0.82 |
| | Mean | 4.22 | 3.05 | 2.93 | 2.72 |

grid products. The 2° × 2.5° lapse rate model performed relatively better in terms of RMSE. Therefore, 2° × 2.5° was selected as the plane resolution of the global grid window.

As shown in Fig. 9, bias and RMSE were higher at high altitudes, similar to the variations in these parameters observed for the MERRA-2 grid product data from the sounding stations. When the GGOS grid Tm elevation correction test was used at exploration sites near Antarctica, the RMSE was relatively high, indicating that the polar day and polar night may affect the lapse rate model. This is consistent with the observation that the lapse rate coefficient had a large annual/semiannual amplitude in the polar region.

### B. Global Tm Grid Model Construction

Most of the existing Tm models use data modeling with single-grid data, which leads to several model parameters and low model efficiency. It is of utmost necessity to establish an efficient Tm model to carry out real-time PWV inversion. The model's efficiency should also be improved as much as possible while ensuring its accuracy. The sliding window algorithm greatly enhances the modeling data utilization by harnessing the Tm data within the joint window range. Moreover, it can effectively reduce the number of modeling parameters and maintain model accuracy. In this study, a global Tm refinement model was developed by adopting a sliding window algorithm based on the directly modeled in-window Tm data. The steps involved in the development of the global Tm refinement model are as follows. Initially, the world was regularly divided based on the sliding window technique to obtain each regular grid window. Since the modeling requires Tm data at the elevation of the window, the MERRA-2 surface Tm grid data in the window should be corrected to the average elevation of each window using the Tm-H1 model. The MERRA-2 surface Tm grid data from 2015 to 2017 for nine grid outlets of each window were corrected to the average elevation of the window. The average elevation of the window is the average value of the elevation of the MERRA-2 grid data in the window, as represented by the following:

$$H_0 = \frac{\sum_{i=1}^{n} H_M^i}{n} \tag{5}$$

where $H_0$represents the average elevation of the window, $H_M^i$ represents the *i*th MERRA-2 lattice elevation in the window, and *n* represents the number of MERRA-2 grids. Thus, the Tm refinement model was developed and represented as( follows:

$$\mathrm{Tm}_{H_0} = \mathrm{Tm}_H + \Delta\mathrm{Tm} \tag{6}$$

$$\mathrm{Tm}_{H_0} = \mathrm{Tm}_{\mathrm{mean}} + \mathrm{amp}_1 \cdot \cos\left(\frac{2\pi}{365.25}(\mathrm{doy} - \varphi_1)\right) \mathrm{amp}_2 \cdot \cos\left(\frac{4\pi}{365.25}(\mathrm{doy} - \varphi_2)\right) \tag{7}$$

where $\mathrm{Tm}_{H_0}$represents the Tm value of $H_0$ at the average elevation, and $\Delta$Tm represents the Tm value at the surface elevation corrected to the average elevation. $\mathrm{Tm}_{\mathrm{mean}}$ represents the annual mean at $\mathrm{Tm}_{H_0}$. $\mathrm{amp}_1$ and $\mathrm{amp}_2$ represent the Tm annual and semiannual cycle amplitudes at the mean window elevation, respectively. $\varphi_1$ and $\varphi_2$ represent annual and semiannual initial phases, respectively. Each parameter of the formed global grid data in the Tm refinement model is stored separately as a file according to the grid plane resolution of 1° × 1.25°. Thus, the Tm model parameters of each window are globally defined, and the global Tm refinement model that can be applied to any height and can be used at high spatial and temporal resolution was finally developed. The global Tm refinement model is abbreviated as the GGTm-H model for convenience in this study.

*1) GGTm-H Model Accuracy Test Using MERRA-2:* MERRA-2 can provide global grid values of Tm. To test the accuracy of the Tm refinement model developed based on the sliding window technique, average daily grid MERRA-2 surface Tm grid data were used to evaluate the accuracy of the GGTm-H model by comparing its Tm values with those from the GPT2w series model and the Bevis model at the same lattice outlets. The bias and RMSE statistics are shown in Table IV.

Table IV shows the distribution of bias and RMSE for different models, with an average bias of 0.21 K for the GGTm-H model, i.e., 1.34 K more than the average bias of the Bevis model. The average bias of GPT2w-5 and GPT2w-1 was 0.07 K and 0.06 K, respectively, possibly because the GPT2w models have high spatiotemporal resolution and a complex grid layout. In addition,

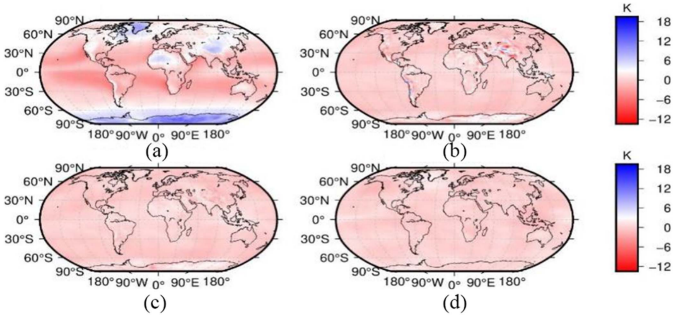


Fig. 10. Distribution of bias of the (a) Bevis, (b) GPT2w-5, (c) GPT2w-1, and (d) GGTm-H models based on the global grid values of MERRA-2 Tm for 2015.

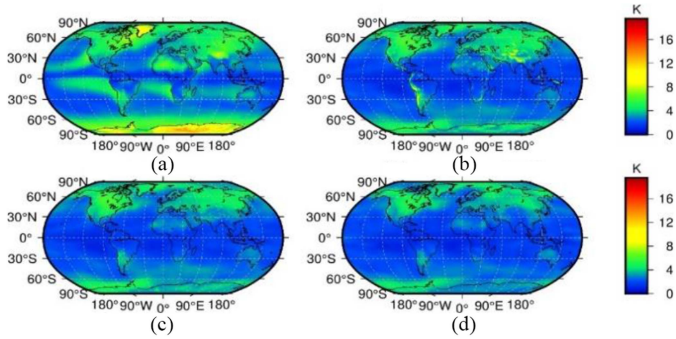


Fig. 11. Distribution of RMSE of the (a) Bevis, (b) GPT2w-5, (c) GPT2w-1, and (d) GGTm-H models based on the global grid values of MERRA-2 Tm for 2015.

all four models had a negative average bias, indicating that the Tm values calculated by the model were low compared to those obtained from MERRA-2 integration. The distribution of bias indicated that the GGTm-H model had the lowest bias values, and its stability was better than that of the other models. The distribution of RMSE indicated that the average RMSE of the GGTm-H model was 2.72 K, i.e., 1.5, 0.33, and 0.21 K more than the average bias of the Bevis, GPT2w-5, and GPT2w-1 models, respectively. This indicated that the developed Tm refinement model using the sliding window technique could estimate Tm with greater accuracy. The Bevis model had the highest RMSE value of 4.22 K, whereas the RMSE values of the GPT2w-5 and GPT2w-1 models were relatively low and stable, i.e., around 3 K.

As shown in Fig. 10, the Bevis model showed a large bias in parts of Antarctica, Greenland, western China, and Africa. As the Bevis model is a regional Tm model developed based on exploration data from North America, it shows a large bias when used to calculate the Tm values on a global scale. The GPT2w-5 model showed a large bias in some regions of western China, Africa, North and South America, and Antarctica. The distribution of bias of the GPT2w-1 model was more uniform than that of the GPT2w-5 model, indicating that the accuracy of Tm estimation can be improved by improving the model's resolution. However, the GPT2w-5 and GPT2w-1 models do not consider the elevation correction when calculating Tm. Therefore, the models' stability is not good in areas with large regional fluctuations. Compared with the other models, the GGTm-H model showed a uniform bias distribution when applied on a global scale. As the model considers the effect of the Tm lapse rate on the elevation correction, it can better estimate the Tm data on a global scale. To conclude, the GGTm-H model significantly outperforms other models on a global scale, with better stability and wide applicability. As shown in Fig. 11, the Bevis model showed the highest RMSE in parts of Antarctica, Greenland, western China, and eastern North America, indicating that a simple linear relationship does not accurately estimate the change in Tm on a global scale. The GPT2w-5 model showed high RMSE in parts of southwest China and western Africa, and the accuracy of the GPT2w-1 model was better than that of the GPT2w-5 model in those regions, indicating that the high-resolution Tm model has certain advantages while calculating Tm. As the GPT2w series

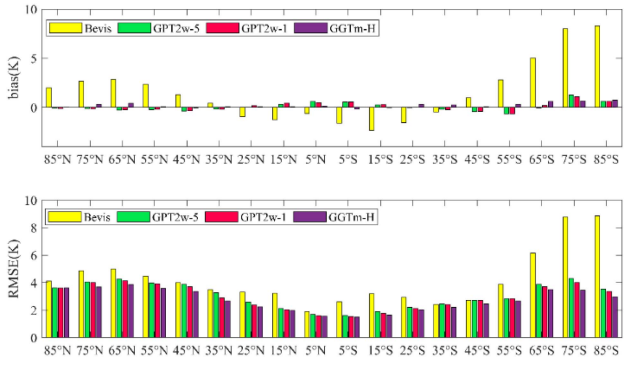


Fig. 12 Verification of bias and RMSE results for the GGTm-H, GPT2w-5, GPT2w-1, and Bevis models at different latitudes based on the global grid values of MERRA-2 Tm.

models do not consider Tm vertical correction for Tm estimation, a high RMSE was observed in these models compared to that in the GGTm-H model. The established GGTm-H model and GPT2w-1 model have comparable accuracy when applied on a global scale; however, the GGTm-H model demonstrated significant improvement in accuracy at high altitude areas, such as southwest China, southern North America, Africa, and parts of Antarctica, indicating that elevation correction can effectively improve the accuracy of Tm estimation in undulating areas.

For evaluating the performance of different models at different latitudes, the global regions were divided into 90°N–180°N and 180°S–90°S, and the variations in bias and RMSE of different models at different latitudes were calculated, as depicted in Fig. 12. The Bevis model showed a significant positive bias at high latitudes and a significant negative bias at 25°N–35°S. The Bevis model showed greater accuracy in the middle latitudes of the northern hemisphere because it mainly relies on the sounding data of this region for validation. Both the GPT2w-5 and GPT2w-1 models showed relatively low average bias at each latitude on a global scale. It is mainly because the GPT2w model has more computational parameters compared with the Bevis model, indicating that the model's performance is relatively stable. The GPT2w model had the highest calculation bias at high latitudes of the southern hemisphere because of the relatively complex spatial and temporal variations in Tm at high latitudes. When compared with the other models, the developed GGTm-H model

TABLE V
ACCURACY OF THE GGTM-H, GPT2W-5, GPT2W-1, AND BEVIS MODELS FOR 319 TM VALUES FOR 2017 (UNIT, K)

| Model | | Bevis | GPT2w-5 | GPT2w-1 | GGTm-H |
|---|---|---|---|---|---|
| bias | Max | 7.42 | 6.14 | 3.54 | 2.64 |
| | Min | –4.46 | –8.61 | –5.24 | –2.14 |
| | Mean | 0.40 | –0.77 | –0.64 | –0.41 |
| RMSE | Max | 9.14 | 9.82 | 6.43 | 6.11 |
| | Min | 1.17 | 1.17 | 1.15 | 1.39 |
| | Mean | 4.62 | 4.18 | 4.01 | 3.82 |

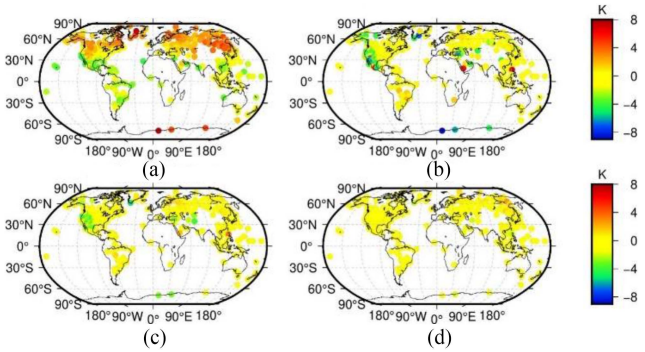


Fig. 13. Distribution of bias values for different models across 319 probe sites for 2017. (a) Bias of the Bevis model. (b) Bias of the GPT2w-5 model. (c) Bias of the GPT2w-1 model. (d) Bias of the GGTm-H model.

had relatively low bias at each latitude, indicating accurate Tm estimation by the model. The RMSE distribution highlighted that each model exhibited a low computation error near the equator, and the RMSE gradually increased with the increasing latitude. The Bevis model showed the highest RMSE at high latitudes of the southern hemisphere, indicating that the regional model introduces large computational errors when used to estimate the global Tm. Compared with the other models, the GGTm-H model showed a relatively low RMSE at each latitude, indicating better model stability and Tm estimation performance.

*2) Precision Test Using RS Data:* RS stations can provide high-precision global Tm data based on the integration method, which can be used to test the applicability of the GGTm-H model on a global scale. As the data from some probe sites were missing, the values from 319 probe sites for 2017 were selected for data analysis to compute the bias and RMSE results daily at UTC 0 and 12. The statistical results are shown in Table V and Figs. 13 and 14. As the Ts values are necessary to compute Tm in the Bevis model, Ts values calculated by the GPT2w-1 model were used for computing Tm in the Bevis model.

As shown in Table V, the bias and RMSE values of the Bevis model ranged from −4.46 to 7.42 K and 1.17 to 9.14 K, with average values of 0.40 K and 4.62 K, respectively. The average bias and RMSE values were −0.77 K and 4.18 K for the GPT2w-1 model, respectively; −0.64 K and 4.01 K for the GPT2w model, respectively; and 0.41 K and 3.82 K for the GGTm-H model, respectively. Compared with the other models, the GGTm-H

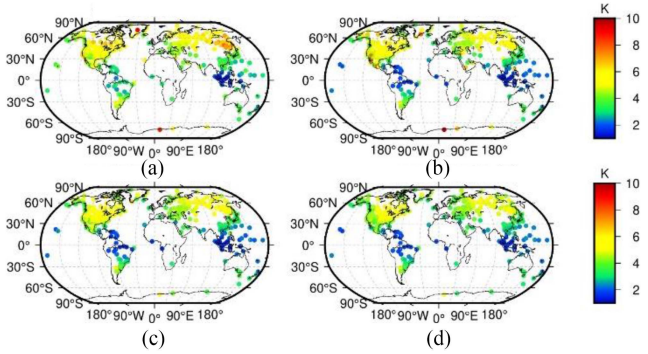


Fig. 14. Distribution of RMSE values for different models across 319 probe sites for 2017. (a) RMSE of the Bevis model. (b) RMSE of the GPT2w-5 model. (c) RMSE of the GPT2w-1 model. (d) RMSE of the GGTm-H model.

model had the lowest annual bias and RMSE, and the variation in error was small, indicating optimal accuracy and stability of the GGTm-H model. When compared with the GPT2w-5 model, the GPT2w-1 model had a low average bias and RMSE and small variations in bias and RMSE, indicating that the GPT2w-1 model performs better than the GPT2w-5 model. Moreover, the high spatial and temporal resolution in the GPT2w-1 model can estimate more accurate Tm values. Both the models have a negative average bias, indicating that the Tm values calculated by the models were less than those obtained from the sounding stations. Compared with the other models, the Bevis model had the highest RMSE. The model formula does not incorporate the periodic changes in Tm, which inevitably leads to uncertainty while calculating the Tm values. As shown in Fig. 13, the Bevis model had a more observable positive bias at higher latitudes and a more significant negative bias near the equator. The Bevis model was built based on the sounding data from North America, and therefore, it may have a large computational bias on a global scale. The GPT2w-5 and GPT2w-1 models showed significantly better accuracy than the Bevis model on a global scale. They showed a significant positive bias at partial GNSS stations near the equator, a significant negative bias near north latitude 30° N, and the highest negative bias in Antarctica. Compared with the other models, GGTm-H had a more uniform bias distribution on a global scale. In addition, the Tm values calculated by the model were found to be more accurate and more consistent with the Tm values obtained from the sounding data. Thus, this signifies the global applicability of the GGTm-H model.

Fig. 14 shows that the Bevis model had the highest RMSE in Greenland and Antarctica, with significant RMSE at high latitudes and lower RMSE at the equator and low latitudes. The RMSE of the Bevis model in parts of North America was smaller than that of the GPT2w-5 model because the Bevis model is constructed from widely distributed sounding data in this region, indicating its applicability to the region. Similar to the Bevis model, the GPT2w-5, GPT2w-1, and GGTm-H models exhibited lower RMSE near the equator and relatively high RMSE at mid- to high-latitudes, implying significant spatiotemporal changes in Tm at high latitudes and thus affecting the model's accuracy. The global RMSE distribution map indicated that the GPT2w-1 model performs better at higher latitudes

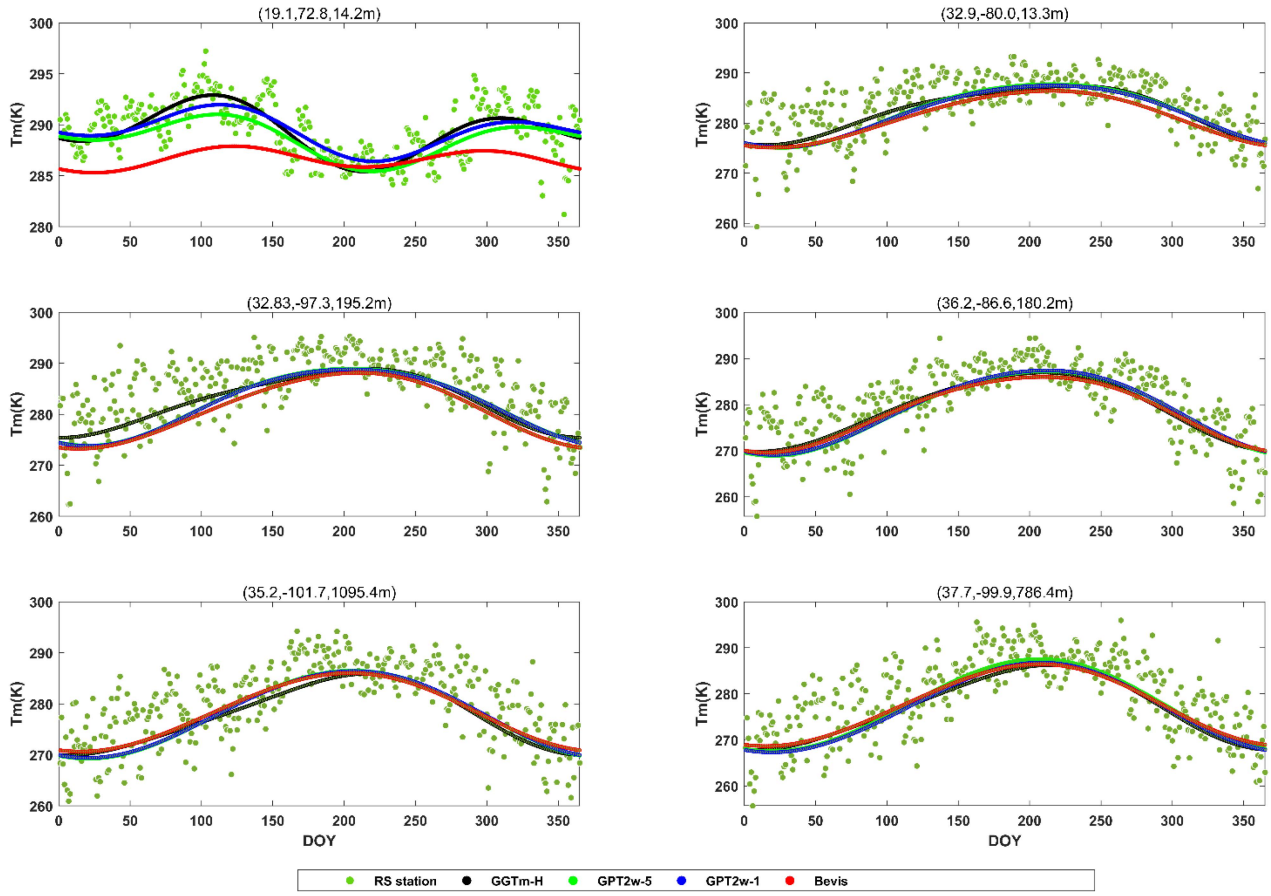


Fig. 15. Comparison of Tm data from different models based on 2017 data (latitude, longitude, and height in parentheses).

than the GPT2w-5 model. The GPT2w-1 model still has a high RMSE compared with the GGTm-H model in the eastern United States. The statistical results presented in Table V reveal that the GGTm-H model is a better model than the other global models and can calculate the Tm value at any position on a global scale with greater accuracy.

To analyze the accuracy of each model at different heights, 319 global sounding sites were arranged in order of their heights, and the bias and RMSE values at different heights were calculated. As shown in Table VI, the average bias of the Bevis, GPT2w-5, GPT2w-1, and GGTm-H models was 0.27, −0.85, −0.59, and −0.36K, respectively, and the average RMSE was 4.59, 4.07, 3.92, and 3.76, respectively, for heights less than 500 m. The variations in bias and RMSE indicate that the GGTm-H model outperformed all the other models and showed the best computational performance and stability among them. When compared with the Bevis model, the bias and RMSE values of the GGZTD-H model were more uniformly distributed. When compared with the GPT2w-5 and GPT2w-1 models, the GGTM-H model showed small variations in annual bias and low RMSE values. The accuracy of the GPT2w-5 and GPT2w-1 models improved to 0.31 and 0.16 K, respectively. The GPT2w-5 and GPT2w-1 models showed small bias and RMSE values at these heights with negative average annual bias, indicating that the Tm values calculated by the model are lower than those calculated by the sounding integral. The accuracy of GPT2w-1 was slightly

TABLE VI
PRECISION OF THE BEVIS, GPT2W-5, GPT2W-1, AND GGTM-H MODELS BASED ON 2017 DATA (UNIT, K)

| | Height (m) | Bevis | GPT2w-5 | GPT2w-1 | GGTm-H |
|---|---|---|---|---|---|
| **b** | ＜500 | [-4.46,7.42] | [-8.61,1.26] | [-5.24,1.39] | [-2.03,1.36] |
| | | 0.27 | -0.85 | -0.59 | -0.36 |
| **i** | 500~ | [-2.89,4.65] | [-6.21,5.98] | [-4.22,3.54] | [-2.14,2.64] |
| **a** | 2000 | 0.96 | -0.75 | -1.07 | -0.72 |
| **s** | ＞2000 | [0.56,7.41] | [1.00,6.14] | [-0.30,1.79] | [-1.64,0.82] |
| | | 3.00 | 3.74 | 0.86 | -0.53 |
| **R** | ＜500 | [1.15,8.71] | [1.17,9.82] | [1.15,6.43] | [1.39~6.11] |
| | | 4.59 | 4.07 | 4.40 | 3.76 |
| **M** | 500~ | [2.42,7.15] | [2.41,7.70] | [2.23,6.11] | [1.88, 5.83] |
| **S** | 2000 | 4.69 | 4.72 | 4.51 | 4.16 |
| **E** | ＞2000 | [3.81,9.14] | [4.32,8.09] | [3.62,5.17] | [3.70,5.08] |
| | | 5.73 | 6.05 | 4.49 | 4.40 |

better than that of GPT2w-5, indicating that the improvement in the horizontal resolution parameters led to an increase in the accuracy of Tm estimation to some extent. Overall, it shows

that the GGTm-H model has good stability at these heights. At 500–2000 m, the average bias of the Bevis, GPT2w-5, GPT2w-1, and GGTm-H models was 0.96, −0.75, −1.07, and −0.72 K, respectively, and the mean RMSE was 4.69, 4.72, 4.51, and 4.16 K, respectively. Due to a small number of statistical sounding stations and contingency errors at heights less than 500 m, the Bevis model performed better than the GPT2w-5 and GPT2w-1 models. However, overall, the GPT2w-1 model performed better than the GPT2w-5 model, and the GGTm-H model showed the most stable model performance. These findings are consistent with the statistical results from the previous studies.

Six RS sites with reliable data were selected to analyze the change in Tm values with time compared to the Tm values obtained by the sounding integral. As shown in Fig. 15, the Bevis model exhibited a relatively large deviation when compared with the other models. Both the GPT2w and GGTm-H models showed a good fit. The Bevis model showed poor performance at low latitudes, and the linear relationship between Tm and Ts was affected by latitude. The GPT2w model incorporates the seasonal characteristics of the troposphere parameters through a function of the annual cycle and semiannual cycle. Therefore, the GPT2w model output depicts noticeable periodic changes. However, the GPT2w model does not consider the elevation correction, resulting in a high bias. In addition, Tm shows seasonal variations, with a maximum in summer of nearly 290 K and a minimum in winter of nearly 260 K in low- and medium-dimensional areas. Compared with RS data, the deviation of the GGTm model is larger in winter and smaller in summer.

## IV. Conclusion

The Tm values computed from the MERRA-2 atmospheric reanalysis data of 294 IGS sites and 545 RS stations have high accuracy and stability and can be used to construct a global multidimensional Tm refinement model.

This study used the sliding window algorithm to evaluate the Tm lapse rate model by calculating global Tm lapse rates from the MERRA-2 reanalysis data at different resolutions and elevations. The result shows that the $2^\circ \times 2.5^\circ$ Tm lapse rate model has good stability. On this basis, we developed a global Tm refinement model, GGTm-H, which can be corrected to any height using the Tm lapse rate model based on the sliding window technique. When compared with other Tm models, the GGTm-H model shows smaller deviation and higher stability over the globe. The validation of the GGTm-H model using MERRA-2 Tm data shows that the RMSE remains stable within 4 K. The validation of the GGTm-H model using RS data shows that the bias is less than −0.72 K and the RMSE remains stable within 4.5 K at the middle and high altitudes, which is far better than the Bevis and GPT models. For any three-dimensional coordinates and time, the Tm value at the average height of the window and the Tm value at the user position can be obtained using the elevation calculation of the Tm lapse rate model. The model is easy to use and can be easily compared to the values obtained by combining the MERRA-2 data and the radio-sounding data.

The sliding window algorithm is adopted in the construction of the GGTm model. Although the data usage efficiency of a single window is increased, the horizontal resolution of model parameters is reduced. How to combine multisource data to determine the global average elevation of each window and refine the model parameters of the tropospheric delay model in each window remains to be further studied.

## Acknowledgment

*Disclaimer:* The authors would like to thank the University of Wyoming for providing the radiosonde profiles (http://www.weather.uwyo.edu/upperair/sounding.html) and the CMA for providing the ground meteorological data (http://data.cma.cn/site/index.html). The reanalysis data, namely, the MERRA-2 products, are provided by NASA (https://goldsmr4.gesdisc.eosdis.nasa.gov/data/MERRA2/).

## References

[1] T. Niksson and G. Elgered, "Long-term trends in the atmospheric water vapor content estimated from ground-based GPS data," *J. Geophys. Res.-Atmos.*, vol. 113, 2008, Art. no. D19101.

[2] J. H. Wang and L. Y. Zhang, "Climate applications of a global, 2-hourly atmospheric precipitable water dataset derived from IGS tropospheric products," *J. Geodesy*, vol. 83, no. 3/4, pp. 209–217, 2009.

[3] R. Christian, V. H. Teresa, and W. Randolph, "Near real-time GPS sensing of atmospheric water vapor," *Geophys. Res. Lett.*, vol. 24, pp. 3221–3224, 1997.

[4] M. D. King, Y. J. Kaufman, W. P. Menzel, and D. Tanre, "Remote sensing of cloud, aerosol, and water vapor properties from the moderate resolution imaging spectrometer," *IEEE Trans. Geosci. Remote Sens.*, vol. 30, no. 1, pp. 2–27, Jan. 1992.

[5] M. Bevis, S. Businger, T. A. Herring, C. Rocken, R. A. Anthes, and R. H. Ware, "GPS meteorology: Remote sensing of atmospheric water vapor using the global positioning system," *J. Geophys. Res., Atmos.*, vol. 97, no. D14, pp. 15787–15801, 1992.

[6] T. R. Emardson, G. Elgered, and J. M. Johansson, "Three months of continuous monitoring of atmospheric water vapor with a network of global positioning system receivers," *J. Geophys. Res.*, vol. 103, no. D2, pp. 1807–1820, 1998.

[7] A. E. Niell, A. J. Coster, and F. S. Solheim, "Comparison of measurements of atmospheric wet delay by radiosonde, water vapor radiometer, GPS, and VLBI," *J. Atmos. Ocean. Technol.*, vol. 18, no. 6, pp. 830–849, 2001.

[8] D. S. Song and D. A. Grejner-Brzezinska, "Remote sensing of atmospheric water vapor variation from GPS measurements during a severe weather event," *Earth, Planets Space*, vol. 61, no. 10, pp. 1117–1125, 2009.

[9] Y. B. Yuan, K. F. Zhang, W. Rohm, S. Choy, R. Norman, and C. Wang, "Real time retrieval of atmospheric water vapour from GPS precise point positioning," *J. Geophys. Res., Atmos.*, vol. 119, no. 16, pp. 10044–10057, 2014.

[10] Y. B. Yao, S. Zhang, and J. Kong, "Research progress and prospect of GNSS space environment science," *Acta Geodaetica et Cartographica Sinica*, vol. 46, no. 10, pp. 1408–1420, 2017.

[11] H. X. Zhang, Y. B. Yuan, W. Li, and B. Zhang, "A real-time precipitable water vapor monitoring system using the national GNSS network of China: Method and preliminary results," *IEEE J. Sel. Topics Appl. Earth Observ. Remote Sens.*, vol. 12, no. 5, pp. 1587–1598, May 2019.

[12] S. Wang et al., "Intercomparison of total precipitable water derived from COSMIC-2 and three different microwave radiometers over the ocean," *IEEE Trans. Geosci. Remote Sens.*, vol. 60, May 2022, Art. no. 4107610.

[13] Q. Z. Zhao, X. W. Ma, W. Q. Yao, and Y. B. Yao, "A new typhoon-monitoring method using precipitation water vapor," *Remote Sens.*, vol. 11, no. 23, 2019, Art. no. 2845.

[14] Q. Z. Zhao, X. W. Ma, and Y. B. Yao, "Preliminary result of capturing the signature of heavy rainfall events using the 2-d-/4-d water vapour information derived from GNSS measurement in Hong Kong," *Adv. Space Res.*, vol. 66, no. 7, pp. 1537–1550, 2020.

[15] L. K. Huang et al., "Spatiotemporal characteristics of GNSS-derived precipitable water vapor during heavy rainfall events in Guilin, China," *Satell. Navigation*, vol. 1, pp. 175–191, 2021.
[16] Y. B. Yao, B. Zhang, C. Q. Xu, and F. Yan, "Improved one/multiparameter models that consider seasonal and geographic variations for estimating weighted mean temperature in ground-based GPS meteorology," *J. Geodesy*, vol. 88, no. 3, pp. 273–282, 2014.
[17] T. Ning et al., "The uncertainty of the atmospheric integrated water vapour estimated from GNSS observations," *Atmos. Meas. Techn.*, vol. 9, no. 1, pp. 79–92, 2016.
[18] J. Wang, L. Zhang, and A. Dai, "Global estimates of water-vapor-weighted mean temperature of the atmosphere for GPS applications," *J. Geophys. Res.*, vol. 110, no. D21, pp. 1–17, 2005.
[19] X. M. Wang, K. F. Zhang, S. Q. Wu, S. J. Fan, and Y. Y. Cheng, "Water vapor-weighted mean temperature and its impact on the determination of precipitable water vapor and its linear trend," *J. Geophys. Res.-Atmos.*, vol. 121, no. 2, pp. 833–852, 2016.
[20] X. Liu et al., "Assessment and calibration of FY-4A AGRI total precipitable water products based on CMONOC," *Atmos. Res.*, vol. 271, 2022, Art. no. 106096.
[21] D. Dee et al., "The ERA-Interim reanalysis: Configuration and performance of the data assimilation system," *Quart. J. Roy. Meteorol. Soc.*, vol. 137, no. 656, pp. 553–597, 2011.
[22] J. H. Wang and L. Y. Zhang, "Systematic errors in global radiosonde precipitable water data from comparisons with ground-based GPS measurements," *J. Climate*, vol. 21, no. 10, pp. 2218–2238, 2008.
[23] J. Wang, A. Dai, and C. Mears, "Global water vapor trend from 1988 to 2011 and its diurnal asymmetry based on GPS, radiosonde, and microwave satellite measurements," *J. Climate*, vol. 29, no. 14, pp. 5205–5222, 2016.
[24] W. X. Zhang et al., "Multiscale variations of precipitable water over China based on 1999–2015 ground-based GPS observations and evaluations of reanalysis products," *J. Climate*, vol. 31, no. 3, pp. 945–962, 2018.
[25] M. Bevis, S. Businger, and S. Chiswell, "GPS meteorology: Mapping zenith wet delays onto precipitable," *J. Appl. Meteorol.*, vol. 33, pp. 379–386, 1994.
[26] H. X. Zhang, Y. B. Yuan, W. Li, J. K. Ou, Y. Li, and B. C. Zhang, "GPS PPP-derived precipitable water vapor retrieval based on $T_m/P_s$ from multiple sources of meteorological data sets in China," *J. Geophys. Res., Atmos.*, vol. 122, no. 8, pp. 4165–4183, 2017.
[27] L. K. Huang, L. L. Liu, H. Chen, and W. P. Jiang, "An improved atmospheric weighted mean temperature model and its impact on GNSS precipitable water vapor for China," *GPS Solutions*, vol. 23, no. 2, 2019, Art. no. 51.
[28] L. K. Huang, W. P. Jiang, L. L. Liu, H. Chen, and S. R. Ye, "A new global grid model for the determination of atmospheric weighted mean temperature in GPS precipitable water vapor," *J. Geodesy*, vol. 93, no. 2, pp. 159–176, 2019.
[29] J. Böhm, G. Möller, M. Schindelegger, G. Pain, and R. Weber, "Development of an improved empirical model for slant delays in the troposphere (GPT2w)," *GPS Solutions*, vol. 19, pp. 433–441, 2015.
[30] Y. B. Yao, S. Zhu, and S. Q. Yue, "A globally applicable, season-specific model for estimating the weighted mean temperature of the atmosphere," *J. Geodesy*, vol. 86, pp. 1125–1135, 2012.
[31] Y. B. Yao, B. Zhang, S. Q. Yue, C. Q. Xu, and W. F. Peng, "Global empirical model for mapping zenith delays onto precipitable," *J. Geodesy*, vol. 87, no. 5, pp. 439–448, 2013.
[32] Y. B. Yao, C. Q. Xu, B. Zhang, and N. Cao, "GTm-III: A new global empirical model for mapping zenith wet delays onto precipitable water vapor," *Geophys. J. Int.*, vol. 197, no. 1, pp. 202–212, 2014.
[33] Y. B. Yao, Z. Y. Sun, and C. Q. Xu, "Applicability of Bevis formula at different height level and global weighted mean temperature model based on near earth atmosphere temperature," *Acta Geodaetica et Cartographica Sinica*, vol. 48, no. 3, pp. 276–285, 2019.
[34] P. Jiang, S. R. Ye, and Y. H. Lu, "Development of time-varying global gridded $T_s$–$T_m$ model for precise GPS–PWV retrieval," *Atmos. Meas. Techn.*, vol. 12, pp. 1233–1249, 2019.
[35] Z. Y. Sun, B. Zhang, and Y. B. Yao, "A global model for estimating tropospheric delay and weighted mean temperature developed with atmospheric reanalysis data from 1979 to 2017," *Remote Sens.*, vol. 11, no. 16, 2019, Art. no. 1893.
[36] Y. B. Yao, Z. Y. Sun, C. Q. Xu, and X. Y. Xu, "Global weight mean temperature model considering nonlinear vertical reduction," *Geomatics Inf. Sci. Wuhan Univ.*, vol. 44, no. 01, pp. 106–111, 2019.
[37] P. Sun, S. Q. Wu, K. F. Zhang, M. F. Wan, and R. Wang, "A new global grid-based weighted mean temperature model considering vertical nonlinear variation," *Atmos. Meas. Techn.*, vol. 14, pp. 2529–2542, 2021.
[38] L. Y. Cao et al., "A regional model for predicting tropospheric delay and weighted mean temperature in China based on GRAPES_MESO forecasting products," *Remote Sens.*, vol. 13, 2021, Art. no. 2644.
[39] I. Durre, R. Vose, and D. B. Wuertz, "Overview of the integrated global radiosonde archive," *J. Climate*, vol. 19, no. 1, pp. 53–68, 2006.
[40] L. K. Huang, G. Zhu, L. L. Liu, H. Chen, and W. P. Jiang, "A global grid model for the correction of the vertical zenith total delay based on a sliding window algorithm," *GPS Solutions*, vol. 25, 2021, Art. no. 98.
[41] G. Zhu, L. K. Huang, Y. Z. Yang, J. Y. Li, L. Zhou, and L. L. Liu, "Refining the ERA5-based global model for vertical adjustment of zenith tropospheric delay," *Satell. Navigation*, vol. 3, 2022, Art. no. 27.
[42] L. K. Huang et al., "High-precision GNSS PWV retrieval using dense GNSS sites and in-situ meteorological observations for the evaluation of MERRA-2 and ERA5 reanalysis products over China," *Atmos. Res.*, vol. 276, 2022, Art. no. 106247.
[43] Q. Z. Li, L. G. Yuan, P. Chen, and Z. S. Jiang, "Global grid-based $T_m$ model with vertical adjustment for GNSS precipitable water retrieval," *GPS Solutions*, vol. 24, 2020, Art. no. 73.
[44] G. Zhu et al., "A new approach for the development of grid models calculating tropospheric key parameters over China," *Remote Sens.*, vol. 13, no. 17, 2021, Art. no. 3546.

**Liangke Huang** received the B.Sc. degree in geomatics engineering and master's degree in geodesy and engineering surveying from the Guilin University of Technology, Guilin, China, in 2011 and 2014, respectively, and the Ph.D. degree in geodesy and engineering surveying from Wuhan University, Wuhan, China, in 2020.

He is currently an Associate Professor with the Guilin University of Technology. His current research interests include GNSS meteorology and tropospheric modeling.

**Zhedong Liu** received the B.Sc. degree in geomatics engineering from the Hubei University of Science and Technology, Xianning, China, in 2019. He is currently working toward the master's degree in geomatics engineering at the Guilin University of Technology, Guilin, China.

His current research interests mainly include GNSS meteorology and tropospheric modeling.

**Hua Peng** received the B.Sc. degree in geomatics engineering from the Hubei University of Science and Technology, Xianning, China, in 2018, and the master's degree in surveying and mapping engineering from the Guilin University of Technology, Guilin, China, in 2021.

His current research interests mainly include GNSS navigation positioning and tropospheric modeling.

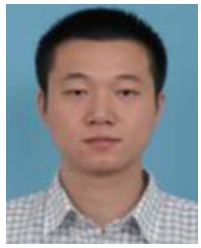

**Si Xiong** received the Ph.D. degree from Wuhan University, Wuhan, China.

He is currently with the School of Resource and Environmental Science and Engineering, Hubei University of Science and Technology, Xianning, China. His research interest includes GNSS meteorology.

**Ge Zhu** received the B.Sc. degree in geomatics engineering from Hubei University of Science and Technology, Xianning, China, in 2019, and master's degree in geomatics engineering from the Guilin University of Technology, Guilin, China, in 2022.

His research interests include GNSS meteorology and tropospheric modeling.

**Fade Chen** received the B.Sc. degree in geomatics engineering and master's degree in surveying and mapping engineering from the College of Geodesy and Geomatics, Guilin University of Technology, Guilin, China, in 2015 and 2018, respectively, and the Ph.D. degree in Geodesy and Engineering Surveying from the School of Geodesy and Geomatics, Wuhan University, Wuhan, China, in 2022.

He is currently a Postdoctoral Researcher with the Guilin University of Technology. His current research focuses on GNSS reflectometry.

**Lilong Liu** received the Ph.D. degree in geodesy and engineering surveying from the School of Geodesy and Geomatics, Wuhan University, Wuhan, China, in 2005.

He is currently a Professor with the Guilin University of Technology, Guilin, China. His main research interests include GNSS data processing, GNSS ionospheric monitoring, and GNSS atmospheric modeling.

**Hongchang He** received the Ph.D. degree in Remote Sensing and Geographic Information from the University of Fribourg, Swiss Confederation, in 2000.

He is a Professor and a National Distinguished expert. He previously engaged in postdoctoral research with Canada's National Remote Sensing Center, which is an internationally renowned research institution. He is the Deputy Team Leader of the "Based on the Polarization Interference of High-Resolution SAR and Multi-Spectral Images for Geological Disaster Information Extraction" project team under the 863 Project of the Ministry of Science and Technology. He led the development of a radar satellite image processing system, which has been chosen by domestic and foreign institutions as a professional tool for radar data processing, marine pollution monitoring, marine disaster warning, and other fields of application software.